Chapter 5

Effective Elastic Micromechanical Damage Model for Bone with Evolutionary Matrix Cracking

5.1 Introduction

Fatigue damage in bone occurs in the form of microcracks. This microdamage acts as a stimulus for bone remodeling. However, if this damage accumulates at such a rate that the capacity for bone repair is exceeded, stress fractures occur. These fractures occur commonly in athletes and soldiers engaged in high intensity, repetitive activities such as marching or running. On the other hand, if damage accumulates at 'normal' rates but the bone's repair mechanism is deficient, fragility fractures result, which occur commonly in aging bone [1]. A combination of cumulative loading history, focal changes in material properties and alteration in the ability of the tissue to perceive and/or react to microcracks may all play roles in this accumulation of bone microdamage with aging. This accumulation of microdamage in bone will contribute to decreased strength and stiffness. In addition, and perhaps most significantly for understanding aging and increased bone fragility, matrix microdamage in bone will result in a profoundly reduced resistance to fracture. The main objective of this chapter is to develop an elastic micromechanical damage formulation for bone material with evolutionary matrix cracking.

5.2 Methods

In the framework of micromechanics, the approximate ensemble-volume averaged compliance for the extravascular bone material with evolutionary matrix cracking can be derived and used to investigate the damage behavior of human bone at the lamellar level.

5.2.1 The Overall Compliance due to the Existence of Penny-Shaped Microcracks

Following Lee and Ju [2], let us consider a two-phase composite composed of a linear elastic matrix and randomly located penny-shaped microcracks. It is assumed that the solid is locally homogeneous and penny-shaped microcracks do not intersect one another. Local homogeneity implies that all probability density function (PDF) do not vary under small translation on a macroscopic length scale. If all penny-shaped microcracks are aligned (parallel) and of equal size, the microcrack-induced perturbed strain of the composite can be expressed as [3, 4]

$$\langle \varepsilon' \rangle (\boldsymbol{x}) = f(\boldsymbol{x}) \int_{S_i} \frac{1}{2} \langle [\boldsymbol{u}] \otimes \boldsymbol{n} + \boldsymbol{n} \otimes [\boldsymbol{u}] \rangle (\boldsymbol{x}' \mid \boldsymbol{x}) \, dS_i \tag{5.1}$$

where "$\otimes$" signifies the tensor expansion; $\boldsymbol{x}'$ denotes a point on the surface (S_i) of a microcrack centered at $\boldsymbol{x}$; $f(\boldsymbol{x})$ is the PDF for a microcrack centered at $\boldsymbol{x}$; and $[\boldsymbol{u}]$ is the vector of microcrack opening displacements. Since all microcracks are aligned (parallel), we can define the microcrack orientation $\boldsymbol{n} = (0,0,1)^T$. For an open penny-

shaped microcrack with radius a embedded in an infinite linear elastic matrix, the microcrack opening displacements at $\boldsymbol{x}'$ (at a distance r from the center of the penny-shaped microcrack) are

$$\begin{Bmatrix} [u'_x] \\ [u'_y] \\ [u'_z] \end{Bmatrix} = \frac{8\left(1-\nu_0^2\right)}{\pi E\left(2-\nu_0\right)}\sqrt{a^2-r^2}\begin{Bmatrix} 2s \\ 2t \\ \left(2-\nu_0\right)p \end{Bmatrix} \tag{5.2}$$

where E and ν_0 are the Young's modulus and Poisson's ratio of the matrix material, respectively; and p, s and t are the z-direction normal, the x-direction shear and the y-direction shear stresses projected on the microcrack surface in its local coordinates as shown in **Figure 5-1**.

Substituting Eq. (5.2) into Eq. (5.1) and carrying out the integration, we obtain

$$\langle \boldsymbol{e}' \rangle(\boldsymbol{x}) = f(\boldsymbol{x})\frac{16\left(1-\nu_0^2\right)}{3E\left(2-\nu_0\right)}a^3\boldsymbol{g}\bullet\langle \boldsymbol{F} \rangle \tag{5.3}$$

where $\langle \boldsymbol{e}' \rangle$ is the microcrack-induced perturbed engineering strain (the Voigt's notation) defined as

$$\langle \boldsymbol{e}' \rangle(\boldsymbol{x}) \equiv \begin{Bmatrix} \langle e'_1 \rangle \\ \langle e'_2 \rangle \\ \langle e'_3 \rangle \\ \langle e'_4 \rangle \\ \langle e'_5 \rangle \\ \langle e'_6 \rangle \end{Bmatrix} = \begin{Bmatrix} \langle \varepsilon'_{xx} \rangle \\ \langle \varepsilon'_{yy} \rangle \\ \langle \varepsilon'_{zz} \rangle \\ 2\langle \varepsilon'_{yz} \rangle \\ 2\langle \varepsilon'_{zx} \rangle \\ 2\langle \varepsilon'_{xy} \rangle \end{Bmatrix} \tag{5.4}$$

The transformation matrix $\boldsymbol{g}$ and the local stress vector $\boldsymbol{F}$ are

$$\boldsymbol{g} = \begin{bmatrix} 0 & 0 & 0 \\ 0 & 0 & 0 \\ 2-\nu_0 & 0 & 0 \\ 0 & 0 & 2 \\ 0 & 2 & 0 \\ 0 & 0 & 0 \end{bmatrix}; \qquad \boldsymbol{F} = \begin{Bmatrix} p \\ s \\ t \end{Bmatrix} \tag{5.5}$$

The local stress vector $\boldsymbol{F}$ is the *superposition* of the unperturbed local stress vector $\boldsymbol{F}^0$ due to remote loading and the local stress perturbation $\tilde{\boldsymbol{F}}$ due to the three-dimensional microcrack interaction.

$$\boldsymbol{F} = \boldsymbol{F}^0 + \tilde{\boldsymbol{F}} = \begin{Bmatrix} p^0 \\ s^0 \\ t^0 \end{Bmatrix} + \begin{Bmatrix} \tilde{p} \\ \tilde{s} \\ \tilde{t} \end{Bmatrix} \tag{5.6}$$

Since the near-field microcrack interaction effects are not considered in this section, we have $\boldsymbol{F} = \boldsymbol{F}^0$. The stress $\boldsymbol{F}^0$ due to far-field loads can be expressed as

$$\boldsymbol{F}^0 = \boldsymbol{K}_0 \bullet \boldsymbol{\sigma}^0 \tag{5.7}$$

where

$$\boldsymbol{K}_0 = \begin{bmatrix} 0 & 0 & 1 & 0 & 0 & 0 \\ 0 & 0 & 0 & 0 & 0 & 1 \\ 0 & 0 & 0 & 1 & 0 & 0 \end{bmatrix}; \qquad \boldsymbol{\sigma}^0 \equiv \begin{Bmatrix} \sigma_{xx}^0 \\ \sigma_{yy}^0 \\ \sigma_{zz}^0 \\ \sigma_{xy}^0 \\ \sigma_{yz}^0 \\ \sigma_{zz}^0 \end{Bmatrix} \tag{5.8}$$

By taking the ensemble average of Eq. (5.7) with $\boldsymbol{F} = \boldsymbol{F}^0$, we arrive at

$$\langle \boldsymbol{F} \rangle = \langle \boldsymbol{K}_0 \rangle \bullet \boldsymbol{\sigma}^0 = \boldsymbol{K}_0 \bullet \boldsymbol{\sigma}^0 \tag{5.9}$$

From Eq. (5.3) and Eq. (5.9), the local microcrack-induced ensemble-averaged perturbed strain at a typical point $\boldsymbol{x}$ can be obtained as

$$\langle \boldsymbol{e}' \rangle (\boldsymbol{x}) = \langle \boldsymbol{S}^{*1} \rangle (\boldsymbol{x}) : \boldsymbol{\sigma}^0 \tag{5.10}$$

where the ensemble-averaged perturbed local compliance reads (assuming a uniform microcrack radius a for simplicity)

$$\langle \boldsymbol{S}^{*1} \rangle (\boldsymbol{x}) = \frac{16\left(1-\nu_0^2\right)}{3E\left(2-\nu_0\right)} f(\boldsymbol{x}) a^3 \boldsymbol{g} \bullet \boldsymbol{K}_0 \tag{5.11}$$

To obtain the volume-ensemble-averaged compliance due to the existence of microcracks within a representative volume element (RVE), we simply apply the volume-average operator to Eq. (5.10) and Eq. (5.11). As a consequence, we have

$$\overline{\langle \boldsymbol{S}^{*1} \rangle} (\boldsymbol{x}) = \frac{1}{V} \int_V \langle \boldsymbol{S}^{*1} \rangle (\boldsymbol{x}) d\boldsymbol{x} = \frac{16\left(1-\nu_0^2\right)}{3E\left(2-\nu_0\right)} \boldsymbol{g} \bullet \boldsymbol{K}_0 a^3 \frac{\int_V f(\boldsymbol{x}) d\boldsymbol{x}}{V} \tag{5.12}$$

Let us assume that there are N microcracks in the RVE; i.e.,

$$\int_V f(\boldsymbol{x}) d\boldsymbol{x} = N \tag{5.13}$$

Substituting Eq. (5.13) into Eq. (5.12), we have

$$\overline{\langle \boldsymbol{S}^{*1} \rangle} = \frac{16\left(1-\nu_0^2\right)}{3E\left(2-\nu_0\right)} \boldsymbol{g} \bullet \boldsymbol{K}_0 \omega \tag{5.14}$$

where $\omega \equiv \frac{Na^3}{V}$ is a parameter representing microcrack concentration. From Equations (5.5), (5.8) and (5.14), we obtain

$$\overline{\left\langle \boldsymbol{S}^{*1} \right\rangle} = \frac{16\left(1-\nu_0^2\right)}{3E\left(2-\nu_0\right)}\omega \begin{bmatrix} 0 & 0 & 0 & 0 & 0 & 0 \\ 0 & 0 & 0 & 0 & 0 & 0 \\ 0 & 0 & 2-\nu_0 & 0 & 0 & 0 \\ 0 & 0 & 0 & 2 & 0 & 0 \\ 0 & 0 & 0 & 0 & 2 & 0 \\ 0 & 0 & 0 & 0 & 0 & 0 \end{bmatrix} \tag{5.15}$$

5.2.2 The Overall Compliance due to the Pairwise Microcrack Interaction

Let us consider two randomly located, aligned, equal-sized, penny-shaped microcracks embedded in a three-dimensional infinite, linear elastic matrix. The local coordinate systems for microcracks 1 and 2 of radius a are shown in **Figure 5-2**. The z-axis is chosen as the direction normal to the microcrack surface. According to the pseudo-traction concept [5], the problem of two interacting microcracks subjected to the far-field stresses can be decomposed into a homogeneous problem and two sub-problems. In the homogeneous problem, a solid without microcracks is subjected to the far-field stresses. In the sub-problem i ($i=1,2$), an infinitely extended solid contains only the i-th penny-shaped microcrack and is subjected to zero remote stress at infinity.

The perturbed normal and shear stress $\tilde{p}_i$, $\tilde{s}_i$, $\tilde{t}_i$ ($i=1,2$) along the surfaces at the microcrack i (i=1,2) location were explicitly derived by Ju and Tseng [5] as

$$\tilde{\boldsymbol{F}}_{1-2} = \tilde{\boldsymbol{K}} \bullet \boldsymbol{F}_{1-2}^{0} \tag{5.16}$$

where $\tilde{\boldsymbol{K}} \equiv \overline{\alpha} \bullet \left(\boldsymbol{I} - \overline{\alpha}\right)^{-1}$. The 6 × 6 microcrack interaction matrix $\overline{\alpha}$ and stress vectors $\tilde{\boldsymbol{F}}_{1-2}$ and $\boldsymbol{F}_{1-2}^{0}$ are shown as followed

$$\bar{\alpha} \equiv \begin{bmatrix} 0 & 0 & 0 & b_3^{(2)} & -c_3^{(2)} & d_3^{(2)} \\ 0 & 0 & 0 & -b_6^{(2)} & c_6^{(2)} & d_6^{(2)} \\ 0 & 0 & 0 & b_5^{(2)} & -c_5^{(2)} & d_5^{(2)} \\ b_3^{(1)} & c_3^{(1)} & d_3^{(1)} & 0 & 0 & 0 \\ b_6^{(1)} & c_6^{(1)} & d_6^{(1)} & 0 & 0 & 0 \\ b_5^{(1)} & c_5^{(1)} & d_5^{(1)} & 0 & 0 & 0 \end{bmatrix} \tag{5.17}$$

$$\boldsymbol{F}_{1-2}^0 \equiv \begin{Bmatrix} p_1^0 \\ s_1^0 \\ t_1^0 \\ p_2^0 \\ s_2^0 \\ t_2^0 \end{Bmatrix}; \qquad \tilde{\boldsymbol{F}}_{1-2} \equiv \begin{Bmatrix} \tilde{p}_1 \\ \tilde{s}_1 \\ \tilde{t}_1 \\ \tilde{p}_2 \\ \tilde{s}_2 \\ \tilde{t}_2 \end{Bmatrix} \tag{5.18}$$

where definitions of the parameters $b_i^{(j)}$, $c_i^{(j)}$ and $d_i^{(j)}$ ($i = 1,2;\ j = 3,5,6$) are summarized in **Appendix III**.

If we define $\tilde{\boldsymbol{F}} = \{\tilde{p}_1, \tilde{s}_1, \tilde{t}_1\}^T$ and $\boldsymbol{K}_1 \equiv$ the first three rows of $\tilde{\boldsymbol{K}}$, the perturbed stresses on the surface of a microcrack due to the existence of the second microcrack can be expressed as

$$\tilde{\boldsymbol{F}} = \boldsymbol{K}_1 \bullet \boldsymbol{F}_{1-2}^0 \tag{5.19}$$

Since the two microcracks under consideration are aligned, it can be easily shown that

$$\boldsymbol{F}_{1-2}^0 \equiv \begin{Bmatrix} p_1^0 \\ s_1^0 \\ t_1^0 \\ p_2^0 \\ s_2^0 \\ t_2^0 \end{Bmatrix} = \begin{bmatrix} 0 & 0 & 1 & 0 & 0 & 0 \\ 0 & 0 & 0 & 0 & 1 & 0 \\ 0 & 0 & 0 & 1 & 0 & 0 \\ 0 & 0 & 1 & 0 & 0 & 0 \\ 0 & 0 & 0 & 0 & 1 & 0 \\ 0 & 0 & 0 & 1 & 0 & 0 \end{bmatrix} \begin{Bmatrix} \sigma_{xx}^0 \\ \sigma_{yy}^0 \\ \sigma_{zz}^0 \\ \sigma_{xy}^0 \\ \sigma_{yz}^0 \\ \sigma_{zz}^0 \end{Bmatrix} \equiv \boldsymbol{K}_2 : \boldsymbol{\sigma}^0 \tag{5.20}$$

From Eq. (5.19) and Eq. (5.20), the perturbed stress vector $\tilde{\boldsymbol{F}}$ over the surface of a microcrack is

$$\tilde{\boldsymbol{F}} = \boldsymbol{K} \bullet \boldsymbol{\sigma}^0 \tag{5.21}$$

where $\boldsymbol{K} \equiv \boldsymbol{K}_1 \bullet \boldsymbol{K}_2$.

The ensemble-averaged local stress perturbation takes the following form

$$\left\langle \tilde{\boldsymbol{F}} \right\rangle (\boldsymbol{x}) = \int_{\Xi} \left\langle \tilde{\boldsymbol{F}} \right\rangle (\boldsymbol{x} \mid \boldsymbol{x}_1) f_1 (\boldsymbol{x}_1 \mid \boldsymbol{x}) d\boldsymbol{x}_1 \tag{5.22}$$

where Ξ designates the open integration domain which depends on the loading conditions, $\left\langle \tilde{\boldsymbol{F}} \right\rangle (\boldsymbol{x} \mid \boldsymbol{x}_1)$ is the ensemble-averaged stress perturbation for a microcrack centered at $\boldsymbol{x}$ over the subclass of realizations having a microcrack centered at $\boldsymbol{x}_1$, and $f_1 (\boldsymbol{x} \mid \boldsymbol{x}_1)$ is the conditional PDF for finding a microcrack centered at $\boldsymbol{x}_1$ given a microcrack centered at $\boldsymbol{x}$.

The conditional PDF $f_1 (\boldsymbol{x} \mid \boldsymbol{x}_1)$ can be further approximated by the PDF for finding a microcrack centered at $\boldsymbol{x}$, $f_1 (\boldsymbol{x})$, if microcracks do not intersect and local homogeneity assumption is true. Consequently, Eq. (5.22) can be simplified as

$$\left\langle \tilde{\boldsymbol{F}} \right\rangle (\boldsymbol{x}) = f_1 (\boldsymbol{x}) \int_{\Xi} \left\langle \tilde{\boldsymbol{F}} \right\rangle (\boldsymbol{x} \mid \boldsymbol{x}_1) d\boldsymbol{x}_1 \tag{5.23}$$

Combining Eq. (5.21) and Eq. (5.23), we arrive at

$$\left\langle \tilde{\boldsymbol{F}} \right\rangle = f_1 (\boldsymbol{x}) \left\langle \boldsymbol{K} \right\rangle : \boldsymbol{\sigma}^0 \tag{5.24}$$

where

$$\left\langle \boldsymbol{K} \right\rangle \equiv \int_{\Xi} \boldsymbol{K} d\boldsymbol{x}_1 = \int_{\Xi} \boldsymbol{K} r^2 \sin\theta dr d\theta d\phi \tag{5.25}$$

The *spherical* coordinate system (r,θ,ϕ) is used to describe the random location $\boldsymbol{x}_1$ of the second microcrack relative to the first random microcrack centered at $\boldsymbol{x}$. Note that θ varies from 0 to π and ϕ ranges from 0 to 2π. If we normalize r with respect to the microcrack radius a (i.e., $\xi \equiv r/a$), then Eq. (5.25) can be recast as

$$\langle \boldsymbol{K} \rangle \equiv a^3 \langle \hat{\boldsymbol{K}} \rangle = a^3 \int_{\Xi} \boldsymbol{K} \xi^2 \sin\theta d\xi d\theta d\phi \tag{5.26}$$

Combining Equations (5.3), (5.24) and (5.26), the local ensemble-averaged perturbed strain (at a typical point $\boldsymbol{x}$) due to the microcrack interaction is

$$\langle \boldsymbol{e}' \rangle (\boldsymbol{x}) = \langle \boldsymbol{S}^{*2} \rangle (\boldsymbol{x}) : \boldsymbol{\sigma}^0 \tag{5.27}$$

where

$$\langle \boldsymbol{S}^{*2} \rangle (\boldsymbol{x}) = \frac{16(1-\nu_0^2)}{3E(2-\nu_0)} f_1^2(\boldsymbol{x}) a^6 \boldsymbol{g} \bullet \langle \hat{\boldsymbol{K}} \rangle \tag{5.28}$$

To obtain the volume-ensemble-averaged compliance due to the microcrack interaction within a RVE, we simply apply the volume-average operator to Eq. (5.28). Consequently, we have

$$\overline{\langle \boldsymbol{S}^{*2} \rangle}(\boldsymbol{x}) = \frac{1}{V} \int_V \langle \boldsymbol{S}^{*2} \rangle (\boldsymbol{x}) d\boldsymbol{x} = \frac{16(1-\nu_0^2)}{3E(2-\nu_0)} \boldsymbol{g} \bullet \langle \hat{\boldsymbol{K}} \rangle a^6 \frac{\int_V f_1^2(\boldsymbol{x}) d\boldsymbol{x}}{V} \tag{5.29}$$

Let us assume that there are N microcracks in the RVE; i.e.,

$$\int_V f_1(\boldsymbol{x}) d\boldsymbol{x} = N \tag{5.30}$$

Furthermore, if the variance of the PDF $f_1(\boldsymbol{x})$ for locations of microcracks is small (e.g., uniform probability), we can have

$$\frac{\int_V f_1^2(\boldsymbol{x})d\boldsymbol{x}}{V} \cong \frac{\left[\int_V f_1(\boldsymbol{x})d\boldsymbol{x}\right]^2}{V} = \frac{N^2}{V} \tag{5.31}$$

Substitution of Eq. (5.31) into Eq. (5.29) then results in

$$\overline{\left\langle \boldsymbol{S}^{*2} \right\rangle} = \frac{16\left(1-\nu_0^2\right)}{3E\left(2-\nu_0\right)} \boldsymbol{g} \bullet \left\langle \hat{\boldsymbol{K}} \right\rangle \omega^2 \tag{5.32}$$

where $\omega \equiv \frac{Na^3}{V}$ is a parameter representing microcrack concentration. From Equations (5.5), (5.26) and (5.32), the overall compliance due to the pairwise microcrack interaction can be obtained.

5.2.3 The Overall Compliance due to the Existence of Inclusions

According to the Eshelby's equivalence principle, the perturbed strain field $\varepsilon'(\boldsymbol{x})$ induced by inhomogeneities can be related to the specified eigenstrain by replacing the inhomogeneities with the matrix material. Following Ju and Chen [6, 7], and Ju and Sun [8, 9], the volume-averaged strain tensor for the two-phase composites can be simplified as

$$\overline{\varepsilon} = \varepsilon^0 + \overline{\varepsilon}' = \varepsilon^0 + \phi \boldsymbol{S} : \varepsilon^* \tag{5.33}$$

where ε^* denotes the eigenstrain, and $\boldsymbol{S}$ signifies the Eshelby's tensor .

If we neglect the near-field inter-inclusion interaction effects, then the solution of eigenstrain ε^* for the single inclusion problem is explicitly expressed as [6]

$$\varepsilon^* = -\left(\boldsymbol{A}+\boldsymbol{S}\right)^{-1} : \varepsilon^0 = -\left[\left(\boldsymbol{A}+\boldsymbol{S}\right)^{-1} \bullet \boldsymbol{C}_0^{-1}\right] : \sigma^0 \tag{5.34}$$

where the fourth-rank tensor $\boldsymbol{A}$ takes the form

$$\boldsymbol{A} = \left[\boldsymbol{C}_1 - \boldsymbol{C}_0\right]^{-1} \bullet \boldsymbol{C}_0 \tag{5.35}$$

Here, $\boldsymbol{C}_0$ and $\boldsymbol{C}_1$ are the stiffness tensors of the matrix and inclusions, respectively. By combining Eq. (5.33) and Eq. (5.34), the resulting first-order approximation of the volume-averaged perturbed strain due to the existence of inclusions becomes

$$\overline{\varepsilon'} = \phi \boldsymbol{S} : \varepsilon^* = -\phi \boldsymbol{S} \bullet \left[\left(\boldsymbol{A} + \boldsymbol{S} \right)^{-1} \bullet \boldsymbol{C}_0^{-1} \right] : \sigma^0 \tag{5.36}$$

Therefore, the corresponding ensemble-volume averaged perturbed compliance tensor, characterizing the first-order contribution due to noninteracting inclusions, takes the form

$$\overline{\left\langle \boldsymbol{S}^{*3} \right\rangle} = -\phi \boldsymbol{S} \bullet \left[\left(\boldsymbol{A} + \boldsymbol{S} \right)^{-1} \bullet \boldsymbol{C}_0^{-1} \right] \tag{5.37}$$

The inverse of fourth-rank tensor can be easily performed using generalized isotropic tensor by Ju and Sun [9]. (cf. **Appendix IV**).

5.2.4 The Overall Compliance and the Microcrack Concentration Evolution

Combining Equations (5.15), (5.32) and (5.37), the overall (volume-ensemble-averaged) effective moduli for a micro-crack-weakened solid (with inclusions) are obtained:

$$\overline{\left\langle \boldsymbol{S} \right\rangle} = \boldsymbol{S}^0 + \overline{\left\langle \boldsymbol{S}^{*1} \right\rangle} + \overline{\left\langle \boldsymbol{S}^{*2} \right\rangle} + \overline{\left\langle \boldsymbol{S}^{*3} \right\rangle} \tag{5.38}$$

$$d\overline{\varepsilon}^e = \overline{\left\langle \boldsymbol{S} \right\rangle} : d\overline{\sigma} \qquad \text{(Stress Driven Formulation)} \tag{5.39}$$

where $\boldsymbol{S}^0$ is the elastic compliance of the matrix.

Since the number of microcracks would increase with the stress level [10] , to characterize the evolution of concentration of microcracks, the following three-parameters formulation is adopted:

$$\omega = A\sigma^B a^3 + C \tag{5.40}$$

where σ is the applied far-field stress, and A, B and C are constants.

5.2.5 Extravascular Bone Material

Within a RVE of extravascular bone material with characteristic length 100 μm, spheroid voids (osteocyte lacunae) which are typically 2 μm in diameter and 6 μm in long axis [11] are embedded in a contiguous matrix built up by the extracellular bone material (Figure 5-3). The effective properties of the extracellular bone material can be obtained through the hierarchical approach developed in Chapter 3 and Chapter 4. The parameters used in the model are listed in **Table 5-1**, which conform to average human lamellar bone.

5.3 Numerical Simulations and Discussions

To demonstrate the capability of proposed framework, comparisons are made between the present theoretical predictions and the experimental data by Ascenzi et al. [12]. According to our review of literature, the microcrack size is generally between 50 to 100 μm. However, at the lamellar level, diffuse damage which is one order or more of magnitude smaller than the microcrack should be considered and regarded as microcrack here.

For mathematical simplicity, the average microcrack radius ($a \cong 0.5$ μm) is adopted. As illustrated in **Figure 5-4** and **Figure 5-5**, when microcrack concentration develops, the overall compliance is increased, making the lamellae more deformable. **Figure 5-6** and **Figure 5-7** show the prediction of the stress-strain curves of the lamella at the initial and final stage of calcification, respectively. It is interesting that there are pre-existing microcracks in both types of lamellae, which may be caused by preparation of the specimens, or suggest that microdamage is present in normal bone tissue in vivo [13]. In addition, from the results, the fully calcified lamella has higher initial microcrack concentraion implying microdamage accumulates with age.

Finally, fully calcified bone has higher stiffness that to be expected, however, fully calcified bone could be quasi-brittle, therefore it may have lower tolerance for microcracks, although the strength is higher.

5.4 Conclusion

To investigate the effects of accumulation of microdamage in bone upon the material properties of lamellae, an elastic micromechanical damage formulation is proposed by incorporating the hierarchical structure concept and evolutionary matrix cracking. It is demonstrated that microdamage exists in bone and contributes to the degradation of bone's material properties. The predicted mechanical behaviors of the lamellae are consistent with the experimental observations in the literature.

5.5 Appendix V: The Parameters b_i, c_i and d_i in Eq. (5.17)

The parameters b_i, c_i, and d_i in Eq. (5.17) take the form [5] :

$$
\begin{aligned}
b_1 &= \frac{2}{\pi}\left[\left(1+2\nu_0\right)k_1 + \frac{az^2}{g_2}k_2\right] \\
b_2 &= \frac{2}{\pi}ag_3^2\left[\left(1-2\nu_0\right)f_2 + \frac{z^2}{g_2}k_3\right]\cos 2\phi \\
b_3 &= \frac{2}{\pi}\left[k_1 - \frac{az^2}{g_2}k_2\right] \\
b_4 &= \frac{2}{\pi}ag_3^2\left[\left(1-2\nu_0\right)f_2 + \frac{z^2}{g_2}k_3\right]\sin 2\phi \\
b_5 &= -\frac{2}{\pi}zg_2g_3k_4\sin\phi \\
b_6 &= -\frac{2}{\pi}zg_2g_3k_4\cos\phi
\end{aligned}
\tag{5.41}
$$

$$
\begin{aligned}
c_1 &= f_3\cos\phi \\
c_2 &= f_4\cos\phi + f_5\cos 3\phi + f_6\left(\cos\phi + \cos 3\phi\right) \\
c_3 &= -2f_6\cos\phi \\
c_4 &= f_4\sin\phi + f_5\sin 3\phi + f_6\left(\sin\phi + \sin 3\phi\right) \\
c_5 &= f_8\sin\phi \\
c_6 &= f_7 + f_8\cos 2\phi
\end{aligned}
\tag{5.42}
$$

$$
\begin{aligned}
d_1 &= f_3\sin 2\phi \\
d_2 &= -f_4\sin\phi + f_5\sin 3\phi + f_6\left(\sin 3\phi - \sin\phi\right) \\
d_3 &= -2f_6\sin\phi \\
d_4 &= f_4\cos\phi - f_5\cos 3\phi - f_6\left(\cos 3\phi - \cos\phi\right) \\
d_5 &= f_7 - f_8\cos 2\phi \\
d_6 &= f_8\sin 2\phi
\end{aligned}
\tag{5.43}
$$

where

$$
\begin{aligned}
f_1 &= \frac{g_1}{g_5}; \quad f_2 = \frac{g_2}{g_5} \\
f_3 &= \frac{4}{\pi\left(2-\nu_0\right)}\left[-2\left(1+\nu_0\right)ag_3f_1 + zg_2g_3k_4\right] \\
f_4 &= -\frac{8\left(1-\nu_0\right)}{\pi\left(2-\nu_0\right)}ag_3f_1 \\
f_5 &= -\frac{8}{\pi\left(2-\nu_0\right)}zg_3f_2g_4^2 \\
f_6 &= \frac{2}{\pi\left(2-\nu_0\right)}zg_2g_3k_4 \\
f_7 &= \frac{2}{\pi}\left(k_1 + \frac{1}{2-\nu_0}zg_1k_2\right) \\
f_8 &= \frac{2}{\pi\left(2-\nu_0\right)}g_3^2\left(\nu_0af_2 + zg_1k_3\right)
\end{aligned}
\tag{5.44}
$$

$$
\begin{aligned}
g_1 &= \left(a^2 - l_1^2\right)^{1/2} \\
g_2 &= \left(l_2^2 - a^2\right)^{1/2} \\
g_3 &= \frac{l_1}{l_2} \\
g_4 &= \frac{a}{l_2} \\
g_5 &= l_2^2 - l_1^2
\end{aligned}
\tag{5.45}
$$

$$
\begin{aligned}
k_1 &= af_2 - \sin^{-1}\left(g_4\right) \\
k_2 &= \frac{l_1^4 + a^2\left(2a^2 + 2z^2 - 3r^2\right)}{g_5^3} \\
k_3 &= \frac{a^2\left(6l_2^2 - 2l_1^2 + r^2\right) - 5l_2^4}{g_5^3} \\
k_4 &= \frac{a^2\left(4l_2^2 - 5r^2\right) + l_1^4}{g_5^3}
\end{aligned}
\tag{5.46}
$$

For the sub-problem 2, ϕ in Equations (5.41), (5.42) and (5.43) is replaced by $\pi - \phi$.

5.6 Appendix VI: An Inverse Formula for the Generalized Isotropic Fourth-Rank Tensor

$$Q_{ijkl} = \left(m + M_{IK}\right)\delta_{ij}\delta_{kl} + \left(w + W_{IJ}\right)\left(\delta_{ik}\delta_{jl} + \delta_{il}\delta_{jk}\right) \tag{5.47}$$

where m and w are constants, whereas, $\boldsymbol{M}$ and $\boldsymbol{W}$ are second-rank tensors. Moreover, $\boldsymbol{W}$ should be symmetric. After some derivations, it can be shown that the inverse of Q_{ijkl} takes the forms:

$$Q^{-1}_{ijkl} = -\frac{Y_{IK}}{2\left(w + W_{II}\right)}\delta_{ij}\delta_{kl} + \frac{1}{4\left(w + W_{IJ}\right)}\left(\delta_{ik}\delta_{jl} + \delta_{il}\delta_{jk}\right) \tag{5.48}$$

where

$$\begin{Bmatrix} Y_{I1} \\ Y_{I2} \\ Y_{I3} \end{Bmatrix} = \begin{bmatrix} m + 2w + M_{11} + 2W_{11} & m + M_{21} & m + M_{31} \\ m + M_{12} & m + 2w + M_{22} + 2W_{22} & m + M_{32} \\ m + M_{13} & m + M_{23} & m + 2w + M_{33} + 2W_{33} \end{bmatrix}^{-1} \begin{Bmatrix} m + M_{I1} \\ m + M_{I2} \\ m + M_{I3} \end{Bmatrix} \tag{5.49}$$

5.7 Appendix VII: Criterion for Microcrack Concentration

The volume of an individual open penny-shaped microcrack with radius a can be estimated by the following equation:

$$V_{crack} \cong \frac{4}{3}\pi a^2 b \tag{5.50}$$

where b is the maximum crack mouth opening displacement.

If there are N microcracks within the representative volume element, the total volume of microcracks must be less than the volume of RVE, that is

$$\frac{N \cdot V_{crack}}{V} \cong \frac{N\frac{4}{3}\pi a^2 b}{V} \leq 1 \tag{5.51}$$

In order to obtain the estimate of the microcrack concentration, we substitute $b = ka$ into Eq. (5.51), which yields

$$\omega = \frac{Na^3}{V} \leq \frac{3}{4\pi k} \tag{5.52}$$

Table 5-1. Set of input parameters for the extravascular bone material

Parameters	Values	Reference
Collagen elastic modulus	2.9 GPa	Sasaki and Odajima [14]
Collagen Poisson's ratio	0.3	-
Apatite crystal bulk modulus	80 GPa	Gilmore and Katz [15]
Apatite crystal shear modulus	45 GPa	Gilmore and Katz [15]
Mineral crystal aspect ratio in fibril	40/3	Akkus [16]
Ultrastructural water and void aspect ratio	1	-
Fibril aspect ratio	100	-
Fibril volume fraction in ultrastructure	0.53	Fritsch and Hellmich [17, 18]
Apatite crystal volume fraction in ultrastructure	0.40 for fully calcified lamella 0.15 for initial stage of calcification	Fritsch and Hellmich [17, 18]
Apatite crystal distribution parameter	0.75	Lees et al. [19] Sasaki et al. [20]
Osteocyte lacunae volume fraction	0.025	Ascenzi et al. [21]
Length of specimens	33 μm	Ascenzi et al. [22] Ascenzi et al. [12] (Figure)
Lamellar width	70 μm	Ascenzi et al. [22]
Lamellar thickness	2 μm	Ascenzi et al. [12]

"Figure" means the value was calculated from a figure in the cited reference

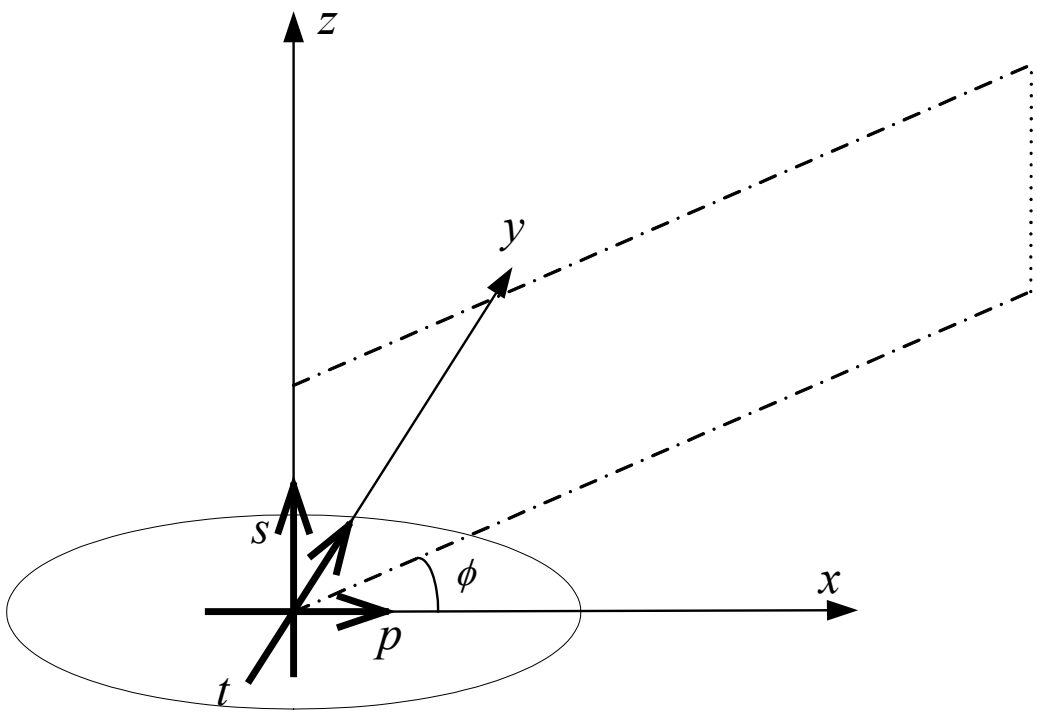

Figure 5-1. A schematic plot of the normal and shear stresses projected on the penny-shaped microcrack surfaces.

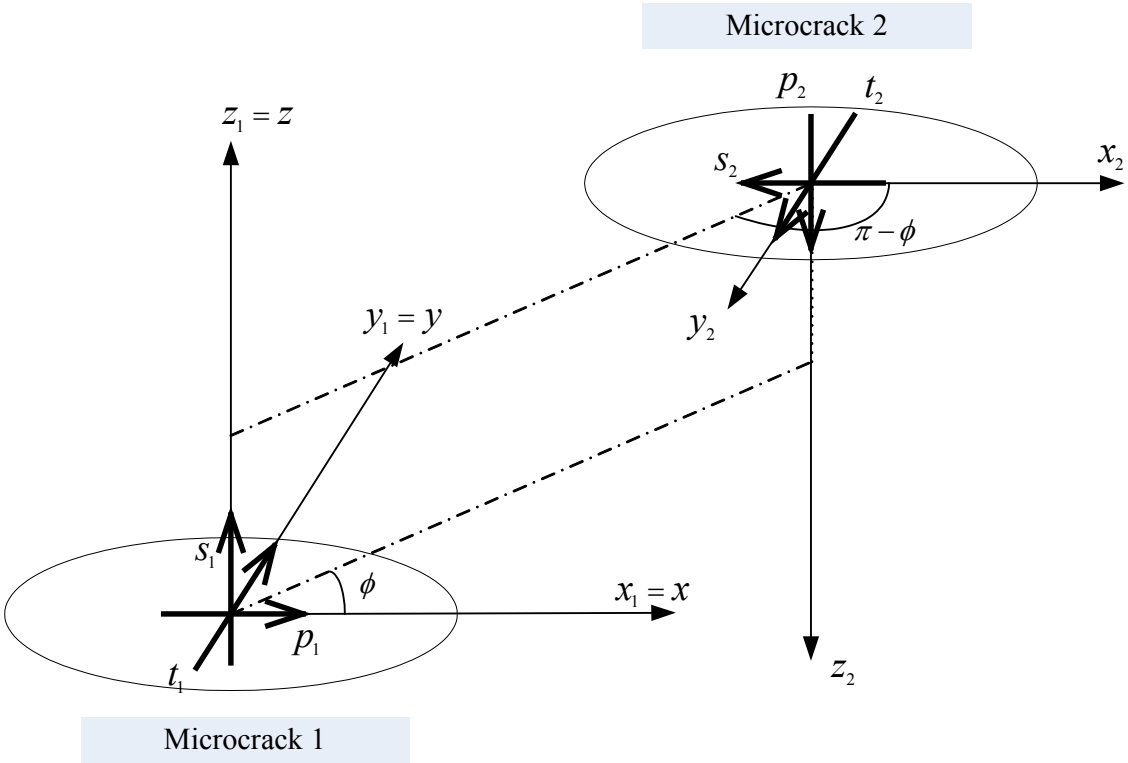

Figure 5-2. The coordinates for two penny-shaped microcracks.

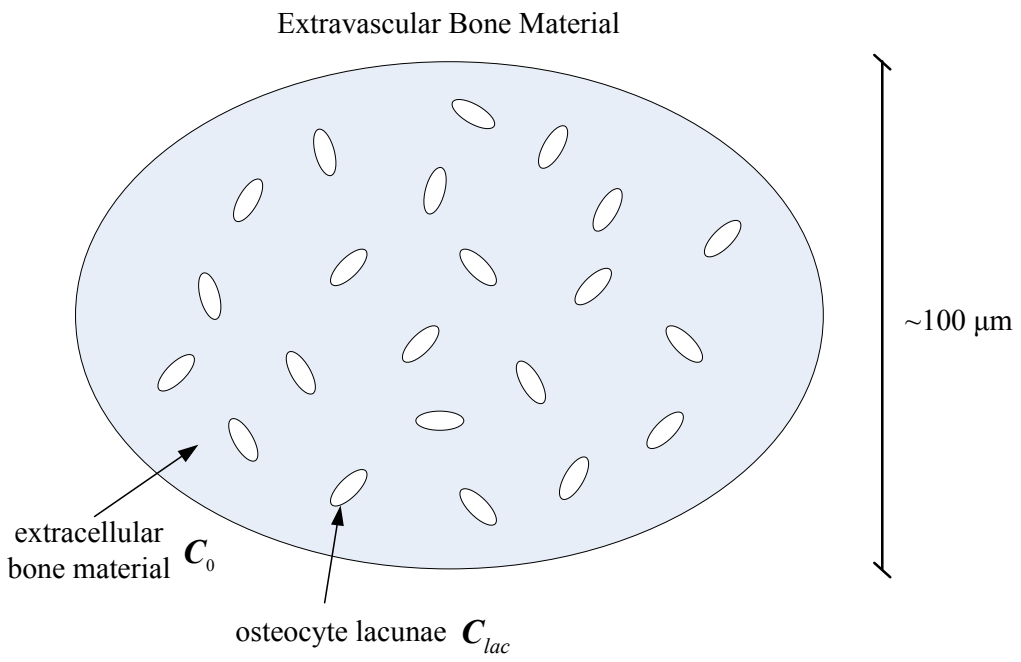

Figure 5-3. Micromechanical representation of extravascular bone material.

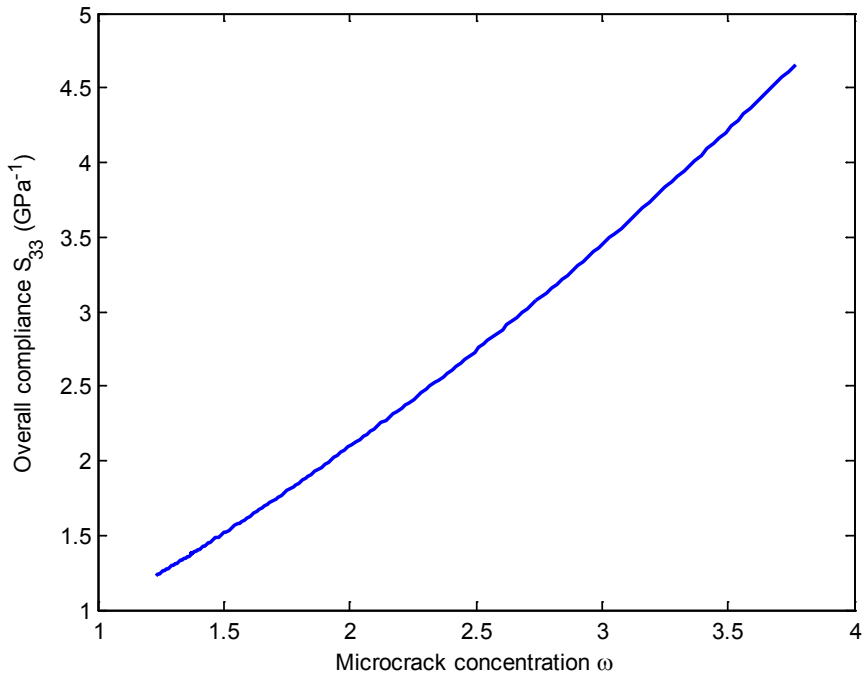

Figure 5-4. The overall compliance S_{33} of the lamella at the initial stage of calcification.

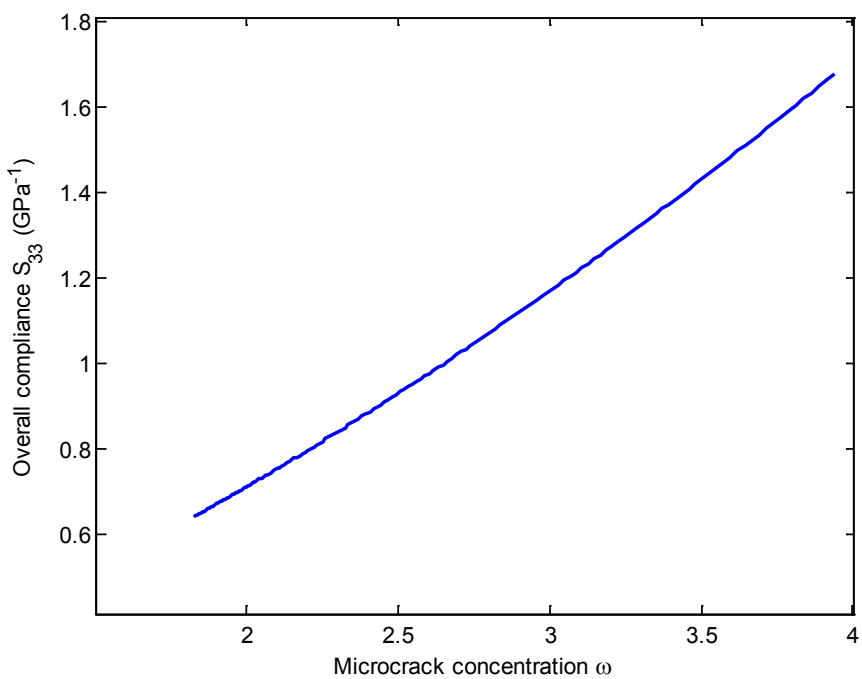

Figure 5-5. The overall compliance S_{33} of the fully calcified lamella.

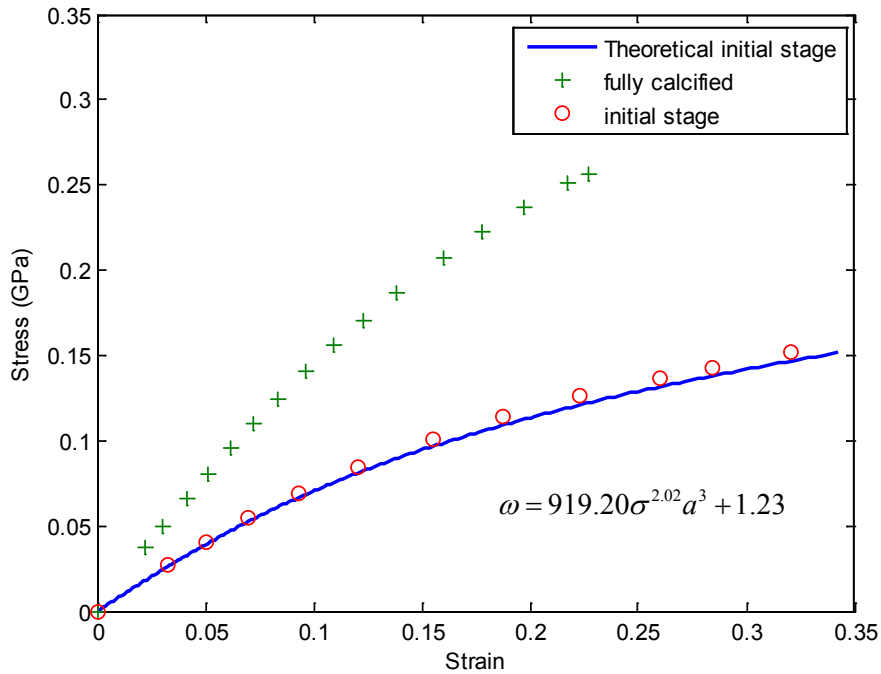

Figure 5-6. The comparison of stress-strain curve of the lamella at the initial stage of calcification.

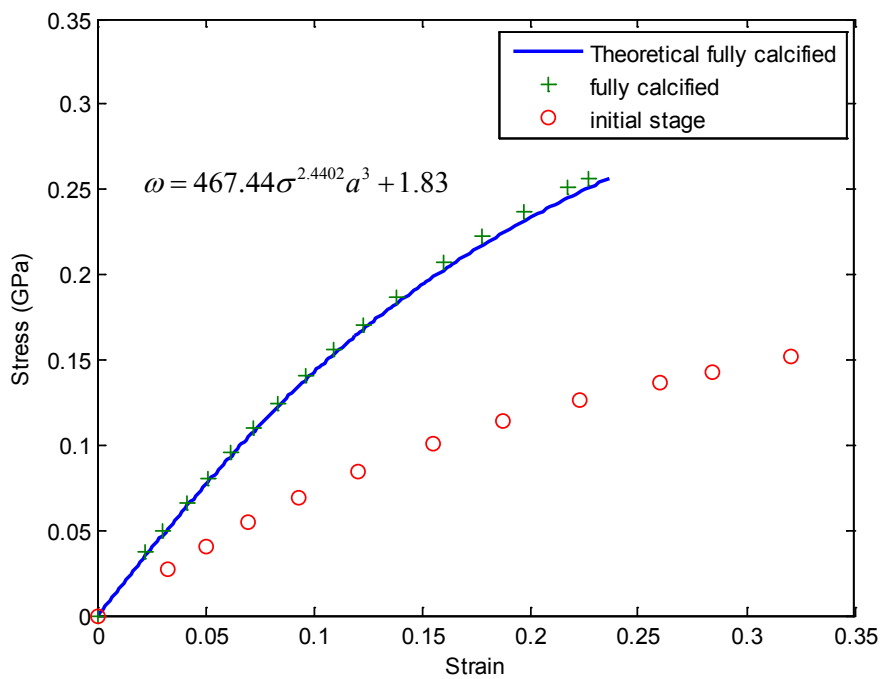

Figure 5-7. The comparison of stress-strain curve of the fully calcified lamella.

5.8 References

1. Schaffler, M.B., K. Choi, and C. Milgrom, *Aging and matrix microdamage accumulation in human compact bone.* Bone, 1995. **17**(6): p. 521-525.
2. Lee, H.K. and J.W. Ju, *3D micromechanics and effective moduli for brittle composites with randomly located interacting microcracks and inclusions.* International Journal of Damage Mechanics, 2008. **17**(5): p. 377-417.
3. Ju, J.W. and K.H. Tseng, *An Improved Two-Dimensional Micromechanical Theory for Brittle Solids with Randomly Located Interacting Microcracks.* International Journal Of Damage Mechanics, 1995. **4**(1): p. 23-57.
4. Nemat-Nasser, S. and M. Hori, *Micromechanics: overall properties of heterogeneous materilas*. Second ed1993, Amsterdam, The Netherlands: Elsevier Science B.V.
5. Ju, J.W. and K.H. Tseng, *A Three-Dimensional Statistical Micromechanical Theory for Brittle Solids with Interacting Microcracks.* International Journal Of Damage Mechanics, 1992. **1**(1): p. 102-131.
6. Ju, J.W. and T.M. Chen, *Micromechanics and effective moduli of elastic composites containing randomly dispersed ellipsoidal inhomogeneities.* Acta Mechanica, 1994. **103**(1-4): p. 103-121.
7. Ju, J.W. and T.M. Chen, *Effective elastic moduli of two-phase composites containing randomly dispersed spherical inhomogeneities.* Acta Mechanica, 1994. **V103**(1): p. 123-144.

8. Ju, J.W. and L.Z. Sun, *A novel formulation for the exterior-point Eshelby's tensor of an ellipsoidal inclusion.* Journal of Applied Mechanics-Transactions of the Asme, 1999. **66**(2): p. 570-574.

9. Ju, J.W. and L.Z. Sun, *Effective elastoplastic behavior of metal matrix composites containing randomly located aligned spheroidal inhomogeneities. Part I: micromechanics-based formulation.* International Journal of Solids and Structures, 2001. **38**(2): p. 183-201.

10. Taylor, D. and T.C. Lee, *Microdamage and mechanical behaviour: predicting failure and remodelling in compact bone.* J Anat, 2003. **203**(2): p. 203-11.

11. McCreadie, B.R., et al., *Osteocyte lacuna size and shape in women with and without osteoporotic fracture.* Journal of Biomechanics, 2004. **37**(4): p. 563-572.

12. Ascenzi, A., A. Benvenuti, and E. Bonucci, *The tensile properties of single osteonic lamellae: Technical problems and preliminary results.* Journal of Biomechanics, 1982. **15**(1): p. 29-37.

13. Burr, D.B., et al., *Bone Microdamage and Skeletal Fragility in Osteoporotic and Stress Fractures.* Journal of Bone and Mineral Research, 1997. **12**(1): p. 6-15.

14. Sasaki, N. and S. Odajima, *Stress-strain curve and young's modulus of a collagen molecule as determined by the X-ray diffraction technique.* Journal of Biomechanics, 1996. **29**(5): p. 655-658.

15. Gilmore, R.S. and J.L. Katz, *Elastic properties of apatites.* Journal of Materials Science, 1982. **V17**(4): p. 1131-1141.

16. Akkus, O., *Elastic deformation of mineralized collagen fibrils: An equivalent inclusion based composite model.* Journal of Biomechanical Engineering-Transactions of the Asme, 2005. **127**(3): p. 383-390.

17. Hellmich, C., J.F. Barthelemy, and L. Dormieux, *Mineral-collagen interactions in elasticity of bone ultrastructure - a continuum micromechanics approach.* European Journal of Mechanics a-Solids, 2004. **23**(5): p. 783-810.

18. Fritsch, A. and C. Hellmich, *`Universal' microstructural patterns in cortical and trabecular, extracellular and extravascular bone materials: Micromechanics-based prediction of anisotropic elasticity.* Journal of Theoretical Biology, 2007. **244**(4): p. 597-620.

19. Lees, S., et al., *The loci of mineral in turkey leg tendon as seen by atomic force microscope and electron microscopy.* Calcified Tissue International, 1994. **55**(3): p. 180-189.

20. Sasaki, N., et al., *Atomic force microscopic studies on the structure of bovine femoral cortical bone at the collagen fibril-mineral level.* Journal of Materials Science-Materials in Medicine, 2002. **13**(3): p. 333-337.

21. Ascenzi, M.-G. and A. Lomovtsev, *Collagen orientation patterns in human secondary osteons, quantified in the radial direction by confocal microscopy.* Journal of Structural Biology, 2006. **153**(1): p. 14-30.

22. Ascenzi, M.-G., J. Gill, and A. Lomovtsev, *Orientation of collagen at the osteocyte lacunae in human secondary osteons.* Journal of Biomechanics, 2008. **41**(16): p. 3426-3435.